



Promising as high-performance supercapacitor electrode materials porous carbons derived from biological lotus leaf

Shanshan Qu, Jiafeng Wan^{*}, Changchao Dai, Tieyu Jin, Fangwei Ma^{**}

School of Chemistry and Material Science, Heilongjiang University, Harbin, 150080, China

ARTICLE INFO

Article history:

Received 7 November 2017

Received in revised form

7 April 2018

Accepted 9 April 2018

Available online 11 April 2018

Keywords:

Supercapacitor

Lotus leaf

Porous carbons

KOH activation

ABSTRACT

The lotus leaf, a renewable source of biomass, was successfully explored as a low-cost crude carbon source for preparing high-value lotus leaf porous carbon (LLPC) via carbonization and KOH activation. The synthesis method is simple, inexpensive and easily scalable. Testing and analysis showed that LLPC is a good supercapacitor electrode material with a microporous and macroporous structure, a specific surface area (SSA) of up to $2488 \text{ m}^2 \text{ g}^{-1}$, and a high content of oxygen heteroatoms. In a three-electrode system with 6 M KOH as the electrolyte, LLPC-800-1:3 exhibited a high specific capacitance of 379 F g^{-1} at 1 A g^{-1} and good rate performance. At a current density of 20 A g^{-1} , the specific capacitance still reached as high as 298 F g^{-1} . Furthermore, after 5000 charging/discharging cycles, the capacitance retention rate was 90%. When the energy density of the electrode was 9.2 Wh kg^{-1} , the power density was 491 W kg^{-1} . The achieved electrochemical performance demonstrates that lotus leaves can function as a new biomass material for the production of high-performance supercapacitors and low-cost energy storage devices.

© 2018 Elsevier B.V. All rights reserved.

1. Introduction

With the rapid growth of the world's population and continuous development of the economy, the demand for efficient energy storage continues to increase, and increasing attention has been paid to energy storage and conversion devices for mobile electronic applications and vehicles [1,2]. As advanced energy storage devices, supercapacitors exhibit extensive application prospects due to their high power density and long cycle life [3–6]. Supercapacitors can be divided into two types according to their energy storage mechanism: pseudo-capacitors and electrical double-layer capacitors (EDLCs) [7]. The capacitance of EDLCs is derived from the electrostatic adsorption of electrolyte ions at the electrode/electrolyte interface [8]. The surface area of the electrode material is a key factor in improving their capacitance: materials with a high SSA provide a large number of active sites, resulting in a high electrical double-layer capacitance [9].

The design of a high-performance supercapacitor mainly depends on the development of efficient electrode materials [10]. To date, carbon materials are the most widely studied and used electrode materials, and they have a large SSA, which has a positive

effect on their electrical storage capability [11]. Through the storage of ions in the electrolyte, an electric double layer is formed at the electrode surface to contribute to the energy storage process [12]. Moreover, the presence of heteroatoms (N, O) present in the carbon-based material can not only improve the pseudocapacitor performance but also improve the wettability and the electrical conductivity of the electrode material [13–16]. Carbon materials include activated carbons (ACs) [17,18], graphene oxide [19,20], carbon nanotubes [21–23], and templated carbons [24,25]. Among these different types of materials, ACs show distinct competitive advantages for use in supercapacitors, including low cost, large SSA and good electrochemical cycling stability [26,27]. AC is prepared primarily by the pyrolysis and activation of biomass precursors, including catkins [28], shrimp shells [29], bark [30], ginkgo leaves [31] and pomelo peel [32]. The microporosity of ACs endows them with high ion-transport resistance and insufficient ionic diffusion within the tortuous micropores; therefore, ACs cannot meet the high power and energy density demands of supercapacitors. Three-dimensional hierarchical porous carbons (3D HPCs) appear to overcome these problems and are considered satisfactory supercapacitors electrode materials. The hierarchical porosity (mesopores in combination with macropores or micropores) of these carbon materials provides both a conducting pathway for electrons and a fast ion-transport channel [33]. The macropores can be used as an ion-buffering reservoir in the interior of the carbon materials [34]. Abundant micropores and mesopores can endow the

^{*} Corresponding author.

^{**} Corresponding author.

E-mail address: wanjiafeng@hlju.edu.cn (J. Wan).

electrode with a highly accessible surface area for enhancing the electrical double-layer capacitance, resulting in a high energy density. The methods for preparing 3D HPCs include template methods [35], a combination of template carbonization and activation [36], and pyrolysis or activation of natural substances [37]. Due to the multiple time-consuming steps and the high cost of the template method, 3D HPCs material cannot be effectively prepared on a large scale. Therefore, obtaining eco-friendly, low-cost novel 3D HPCs from a renewable biomass is important.

Biomass often refers to the various organisms that perform photosynthesis, including all animals, plants and microbes. As a carbon-rich precursor, biomass has consistently been a sustainable source of carbon materials. The traditional method of synthesis is based on a combination of direct pyrolysis and activation methods; thus, the resulting material is referred to as AC [38]. The method used to prepare biomass carbon has a significant influence on the pore structure (macropores, mesopores and micropores), SSA, surface functional groups and graphitization degree [39]. To control the structure and properties of the obtained carbon materials, new methods for the synthesis of carbon materials have been proposed, including hydrothermal carbonization, molten salt carbonization and template methods [40–42]. However, because some of the abovementioned methods for synthesizing carbon materials are expensive and time-consuming, we have developed a low-cost and simple method for producing lotus leaf porous carbon (LLPC). This method can produce LLPC on a large scale and has great commercial potential.

Lotus leaves undergo many years of aquatic herb growth. Lotus plants have great therapeutic value; for example, lotus leaf tea has a good weight loss effect. However, the waste residue of lotus leaf is often discarded, resulting in abundant waste. Therefore, we must make use of this waste. In this study, we used lotus leaf tea residue as a carbonization precursor and then used KOH as an activator to prepare a porous carbon (PC) material. The obtained LLPC material has a high SSA of $2488 \text{ m}^2 \text{ g}^{-1}$. In a three-electrode system with an alkaline solution (6 M KOH) used as the electrolyte, the material demonstrated a high capacitance of 379 F g^{-1} at 1 A g^{-1} . The material exhibited good cycling stability and a capacitance retention rate of 90% after 5000 charge/discharge cycles. In 1 M Na_2SO_4 electrolyte, at a power density of 868 W kg^{-1} , a high energy density of 23 W h kg^{-1} was observed.

2. Experimental

2.1. Preparation of LLPC

The materials used in this experiment were residues of lotus leaf tea. The lotus leaves were washed and then dried for 12 h at 80°C . After drying, the leaves were pre-carbonized at 500°C for 1 h under a protective atmosphere of nitrogen gas at a heating rate of 5°C min^{-1} . The carbonized samples were uniformly milled with KOH (the mass ratio of the material to KOH was 1:3). Then, the samples were placed in a tube furnace and calcined at 700°C , 800°C , or 900°C for 1 h, and the samples obtained by calcining at different temperatures were recorded as LLPC-700-1:3, LLPC-800-1:3, and LLPC-900-1:3, respectively. The pre-carbonized sample and KOH were uniformly milled in a ratio of 1:2 or 1:4 and calcined at 800°C for 1 h. The other preparation steps were the same as those indicated above, and the porous carbon samples prepared with sample KOH ratios of 1:2 and 1:4 were labelled LLPC-800-1:2 and LLPC-800-1:4, respectively.

2.2. Morphological and microstructural characterization

In this experiment, a Hitachi S-4800 scanning electron

microscope (SEM) was used to characterize the morphology of the LLPC. The microstructure of the LLPC was observed under a JEOL-2100 transmission electron microscope (TEM) at JEOL. The microcrystalline structure was determined by a D8 Advance powder X-ray diffractometer (XRD) with $\text{Cu K}\alpha$ radiation ($\lambda = 1.5406 \text{ \AA}$) between 10° and 80° at a scan rate of 0.02° . The nitrogen adsorption-desorption isotherm of a sample was measured on a Quadachrome adsorber at 77 K , and the total SSA of the sample was calculated by the Brunauer-Emmett-Teller (BET) method. The pore size distribution was obtained by density functional theory (DFT). X-ray photoelectron spectroscopy (XPS) was carried out by using a VG ESCALAB MK II X-ray photoelectron spectrometer (VG Scientific). An HR800 type laser Raman spectrometer was used to test the sample at an excitation wavelength of 458 nm .

2.3. Electrochemical performance

To measure the electrochemical properties of the LLPC, an electrode was first prepared. The LLPC, acetylene black and poly(tetrafluoroethylene) were mixed in a ratio of 80:10:10, and the mixture (2.0 mg cm^{-2}) was pressed at 8 MPa on nickel foam ($1 \times 1 \text{ cm}^2$) to form a working electrode. Electrochemical measurements were sequentially performed in a KOH solution and a NaOH solution using a CHI660E electrochemical workstation. During fabrication, the LLPC-acetylene black-poly(tetrafluoroethylene) electrodes, platinum and Ag/AgCl were used as the working electrode, the counter electrode and the reference electrode, respectively. Cyclic voltammetry (CV) analysis was performed in alkaline solution (6 M KOH) over a potential range of -1 – 0 V , a galvanostatic charge-discharge (GCD) test voltage of -1 – 0 V , an electrochemical impedance spectroscopy (EIS) frequency range of 0.1 – $1 \times 10^5 \text{ Hz}$, and an amplitude of 5 mV . The specific gravimetric capacitance was calculated by the following formula:

$$C_s = \frac{I\Delta t}{m\Delta V}$$

where m (g) is the mass of AC, ΔV (V) is the voltage change (not including the IR decrease during the discharge process), I (A) is the current density, and Δt (s) is the discharge time.

In the two-electrode system, the working voltage range of the CV test and GCD test was 1 – 0 V , and the specific capacitance of a single electrode was calculated according to the following formula:

$$C_s = \frac{4I\Delta t}{m\Delta V}$$

The energy density (E_t) and the power density (P_t) of the symmetric supercapacitor system were calculated using the following equations:

$$E_t = \frac{C_t(\Delta V)^2}{2 \times 3.6}$$

$$P_t = \frac{E_t}{t} \times 3600$$

3. Results and discussion

The surface morphology of the LLPC was characterised by scanning electron microscopy (SEM). Fig. 1a shows that the pre-carbonized sample occurred in the form of a sheet and possessed a smooth surface. As shown in Fig. 1b, KOH etching of the LLPC led to the formation of an extremely rough surface. The rough surface

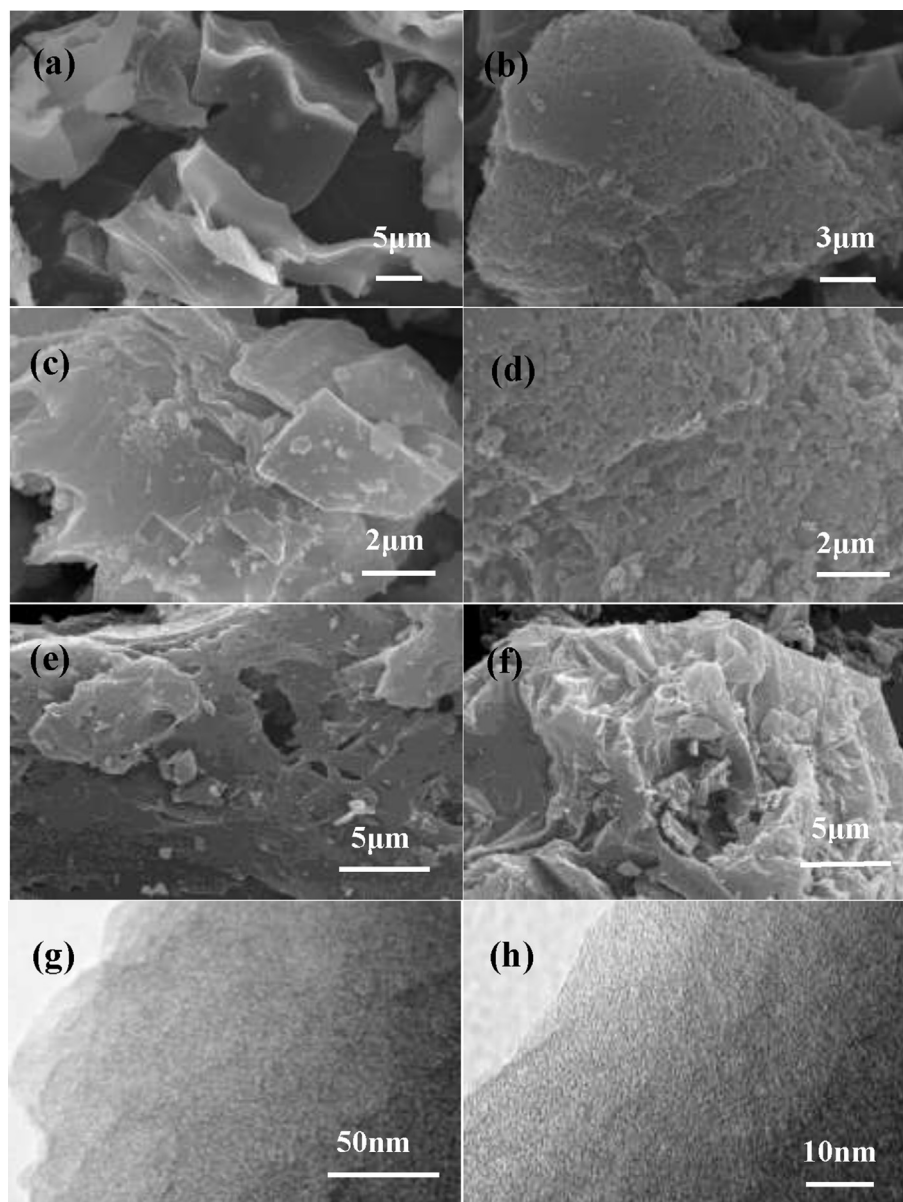


Fig. 1. (a, c) SEM images of lotus leaf material without KOH activation after pre-carbonization. (b, d) SEM images of LLPC-800-1:3. (e, f) SEM images of LLPC-700-1:3 and LLPC-900-1:3. (g, h) TEM images of LLPC-800-1:3.

of the activated sample can store a large amount of charge, therefore increasing the electron transport ability. A high level of magnification was used to more clearly observe the sample via SEM (Fig. 1c and d), demonstrating the changes in the morphology of the LLPC with and without activation. Fig. 1c shows that the pre-carbonized sample featured a lamellar structure and that no pores were present at the surface. The surface morphology of the LLPC after KOH activation changed significantly, as shown in Fig. 1d, and many interconnected macropores were observed on the surface of the LLPC. The interconnected macropores contained in the material are important because they can help in improving the transfer of ions by providing pathways for the transport and permeation of electrolyte ions. Fig. 1e shows an SEM image of LLPC-700-1:3, demonstrating a relatively rough surface. The surface of this LLPC showed abundant debris, therefore increasing its roughness (Fig. 1f). As the activation temperature increases, the reaction between carbon and KOH may become more intense. SEM images of LLPC-800-1:2 and LLPC-800-1:4 are shown in Fig. S1. Fig. S1a

shows that the surface of LLPC-800-1:2 was relatively rough, and the surface of LLPC-800-1:4 in Fig. S1b was etched from a large number of concave surfaces. As the amount of KOH activator increased, the LLPC surface was etched more severely.

The microstructure of the LLPC was characterised by transmission electron microscopy (TEM). Fig. 1g and h shows the lamellar structure of the LLPC, which is in agreement with the SEM results. TEM images of LLPC-800-1:2 and LLPC-800-1:4 are shown in Fig. S2. These TEM images show that KOH activation led to a uniform distribution of a large number of worm-like micropores on the carbon sheet. Micropores can enhance the electrical double-layer capacitance, and the presence of numerous micropores can contribute greatly to the high SSA of the LLPC [43]. All of the above mentioned results demonstrate that LLPC is a good electrode material for high-performance supercapacitors.

The N_2 adsorption isotherms and the pore sizes of the LLPC were measured using nitrogen adsorption-desorption measurements. As shown in Fig. 2a, all of the LLPCs exhibited a clear type I adsorption-

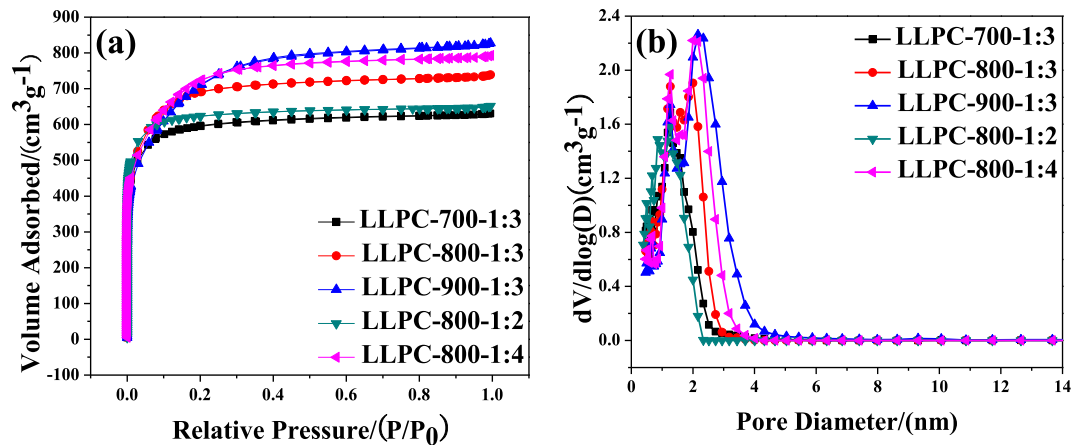


Fig. 2. (a) Nitrogen absorption/desorption isotherms and (b) corresponding pore size distribution plots of the LLPC.

desorption isotherms. The N_2 adsorption isotherms sharply increased at low relative pressures, indicating that the LLPCs contained numerous micropores. As the processing temperature increased, the volume of the adsorbed N_2 gas increased when the relative pressure (P/P_0) was ~ 1 . Fig. 2b shows the pore size distribution of the LLPC material. The pore networks of LLPC-700-1:3 and LLPC-800-1:3 mainly consisted of micropores, whereas the pore networks of LLPC-900-1:3 and LLPC-800-1:4 mainly contained micropores and small mesopores (2–3 nm). A large number of micropores in the LLPC materials led to the increased SSAs, providing more active sites for charge accumulation and thus higher electrical double-layer capacitance. The SSAs of LLPC-700-1:3, LLPC-800-1:3 and LLPC-900-1:3 were $2297 \text{ m}^2 \text{g}^{-1}$, $2489 \text{ m}^2 \text{g}^{-1}$ and $2488 \text{ m}^2 \text{g}^{-1}$, respectively, and the pore volumes were 0.98, 1.14 and $1.28 \text{ cm}^3 \text{g}^{-1}$, respectively. As the temperature increased, the micropore surface area and micropore volume of the

LLPC decreased gradually. The specific properties of the LLPC materials are summarized in Table 1. The collapse of the micropores in the material led to the formation of small mesopores and may have been due to the increase in the activation temperature. Table 1 shows that as the activator content increased, the SSA increased, whereas the micropore surface area and micropore volume of the LLPC decreased gradually. These results demonstrate that the LLPC was etched more severely with increasing KOH content. The collapse of the micropores in the material led to the formation of small mesopores. A porous structure in which mesopores and micropores coexist is desirable. Mesopores can also facilitate high adsorbate accessibility by providing wider transport channels than those provided by micropores [44].

The X-ray diffraction (XRD) patterns of the LLPCs are shown in Fig. 3a. All the LLPCs showed a broad peak at $2\theta = 24.8^\circ$ and a weak peak at $2\theta = 42.9^\circ$, which correspond to the (002) and (110) planes

Table 1
Pore characteristics of various LLPCs.

Samples	$S_{\text{BET}} [\text{m}^2 \text{g}^{-1}]$	$S_{\text{micro}} [\text{m}^2 \text{g}^{-1}]$	$V_{\text{pore}} [\text{cm}^3 \text{g}^{-1}]$	$V_{\text{micro}} [\text{cm}^3 \text{g}^{-1}]$	$D_{\text{aver}} [\text{nm}]$
LLPC-700-1:3	2297	1870	0.97	0.73	2.61
LLPC-800-1:3	2488	1456	1.14	0.61	2.41
LLPC-900-1:3	2487	405	1.28	0.18	2.41
LLPC-800-1:2	2446	2091	1.01	0.81	2.45
LLPC-800-1:4	2533	853	1.23	0.38	2.37

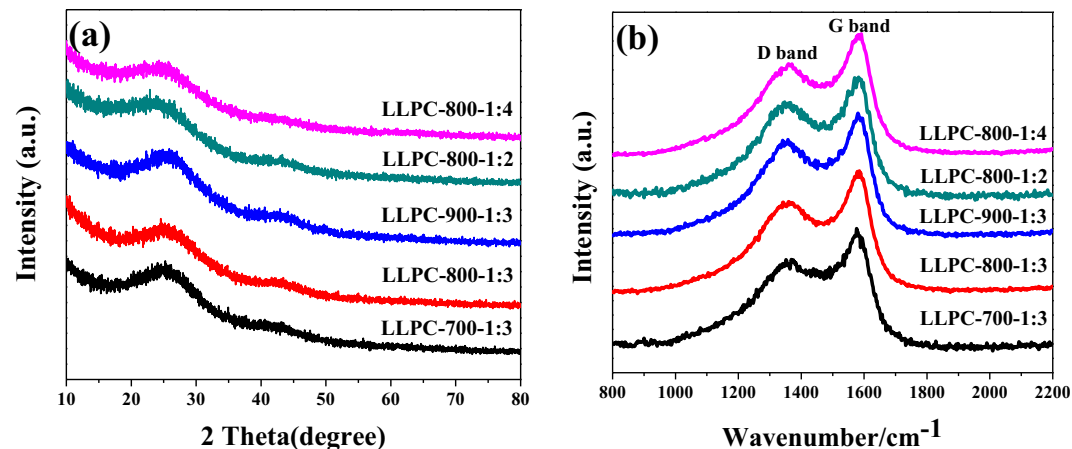


Fig. 3. (a) XRD patterns of the LLPC and (b) Raman spectra of the LLPC.

Table 2

Chemical composition of LLPC determined by XPS.

Samples [mass%]	C 1s [mass%]	O 1s [mass%]	N 1s [mass%]
LLPC-700-1:3	90.22	9.11	0.68
LLPC-800-1:3	93.84	5.34	0.83
LLPC-900-1:3	88.74	10.46	0.80
LLPC-800-1:2	90.88	7.10	2.02
LLPC-800-1:4	90.39	8.64	0.97

of the graphite structure, respectively [45]. The observed diffraction pattern indicate that the prepared AC mainly contains a significant amount of amorphous carbon [46]. As the temperature increased, the (002) peak became narrower, indicating an ordering process in the mainly amorphous carbon [47]. As shown in Fig. 3b, the Raman spectra of LLPC-700-1:3, LLPC-800-1:3 and LLPC-900-1:3 display two characteristic absorption peaks at 1368 cm^{-1} (D peak) and 1576 cm^{-1} (G peak). The D-band peak is the characteristic absorption peak of amorphous carbon, and the G-band peak is related to the distribution of sp^2 hybridized carbon atoms in the graphite carbon phase. The intensity ratio of the D peak to the G peak (ID/IG) is commonly used to measure the degree of graphitization and the degree of disorder of carbon materials [48]. The ID/IG values of LLPC-700-1:3, LLPC-800-1:3, and LLPC-900-1:3 were 0.79, 0.79, and 0.82, respectively. It is known that the greater the ratio is, the lower is the degree of graphitization becomes. Therefore, increasing the processing temperature facilitates disorder and decreases the degree of graphitization in a sample [49,50]. The ID/IG values for LLPC-800-1:2 and LLPC-800-1:4 were 0.83 and 0.79, respectively, indicating that the degree of graphitization increased as the amount of KOH activator increased.

The elemental composition of the surface and heteroatom content of heteroatoms in the LLPCs were measured using X-ray photoelectron spectroscopy (XPS). The materials contained three elements, carbon, nitrogen and oxygen; their contents are shown in Table 2. The materials contained a small amount of nitrogen, which may have resulted from the carbon material itself containing a small amount of nitrogen atoms or from the introduction of nitrogen during the high-temperature process. The C content in the material reached 90.2%, indicating that the yield of PC was high. Fig. 4a shows the characteristic C 1s, O 1s, and N 1s peaks of the materials. Strong C 1s and O 1s peaks arose at 290 eV and 537 eV, respectively, and a weak N 1s peak arose at 407 eV. Fig. 4b and c show the peaks assigning for C 1s and O 1s, with C 1s peaks appearing at 284.6 eV (C=C), 287.8 eV (C=O), and 285.5 eV (C–C) [51–53]. The O 1s peaks occur at 534.9 eV (–O–), 533.7 eV (C–O–C), and 532.5 eV; the last of these three peaks is attributed to either alcohol, phenol, aliphatic ether, or other compounds containing hydroxyl groups (C–OH) [54–56]. The results obtained for the O 1s and C 1s peaks of LLPC-800-1:2 and LLPC-800-1:4 are shown in Fig. S3. These abundant functional groups can improve the wettability of the material and thus increase the activity of the SSA.

In this study, the electrochemical properties of LLPC were characterised using a three-electrode system and 6 M KOH as the electrolyte. The CV curves of the samples were measured at a scan rate of 20 mV s^{-1} (Fig. 5a). As the temperature increased, the CV curves of the samples became more rectangular. The CV curve of LLPC-700-1:3 appeared convex at $-1-0.4\text{ V}$, resulting in a deviation from the rectangular shape, which may be attributed to the redox peaks of the heteroatoms. Another factor is the resistance to the diffusion of the ions in electrolyte in the micropores; moreover, when a loop is completed, ion diffusion is delayed, resulting in a delay in the current response. The resulting dispersion capacitance

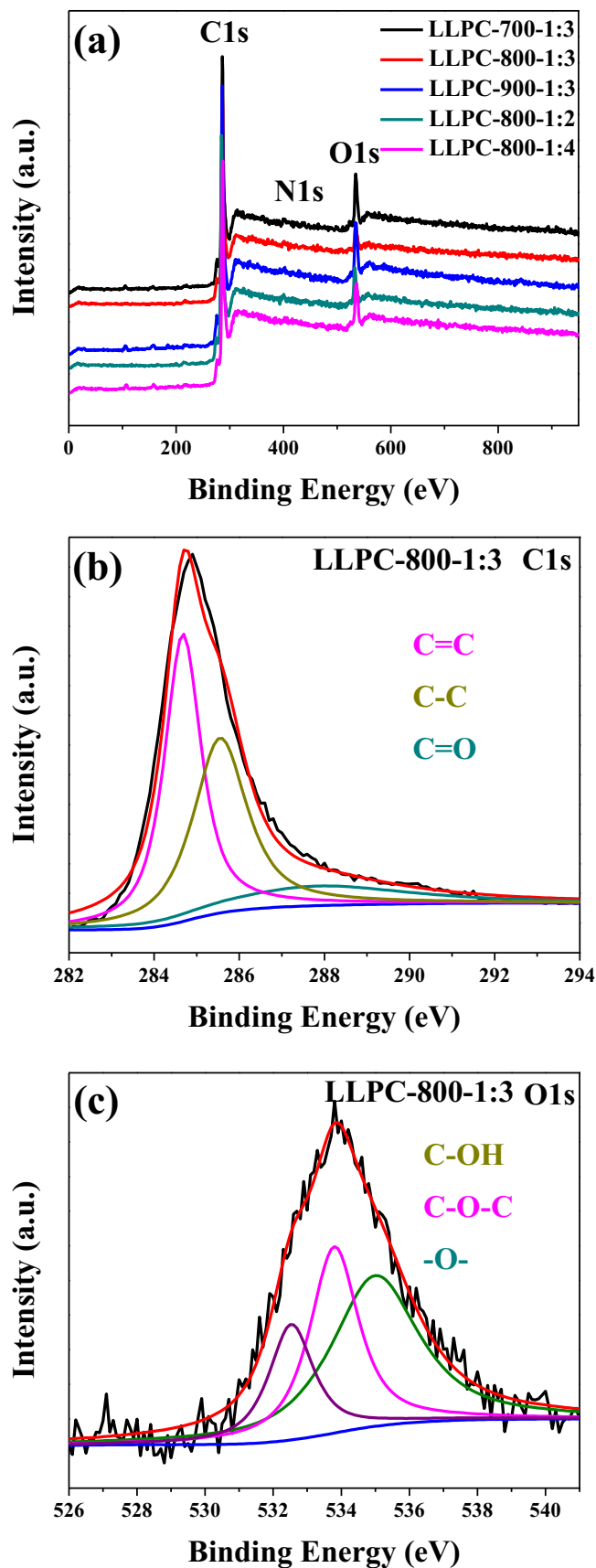


Fig. 4. (a) XPS survey spectra of the LLPC and C 1s (b) and O 1s (c) XPS spectra of LLPC-800-1:3.

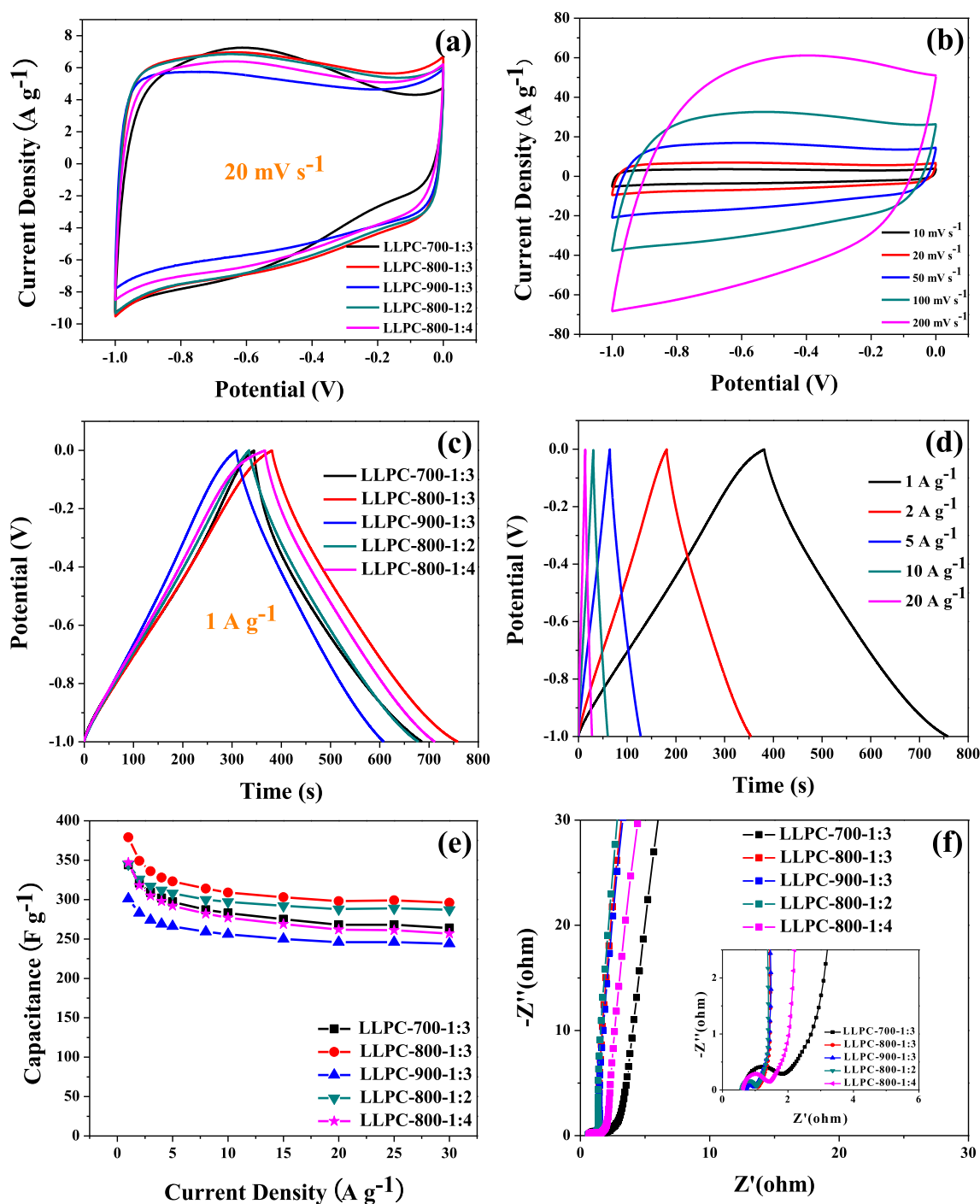


Fig. 5. Electrochemical performance characteristics of the LLPC measured in a three-electrode system in 6 M KOH electrolyte: (a) CV curves at 20 mV s^{-1} ; (b) CV curves of LLPC-800-1:3 at different scan rates, (c) GCD curves at a current density of 1 A g^{-1} , (d) GCD curves of LLPC-800-1:3 at different current densities, and (e) specific capacitance values of LLPC at different current densities, and (f) Nyquist plots over the frequency range of 10 kHz to 10 mHz.

effect generated a CV curve that deviated from the rectangular shape. The pore structure test illustrates that with an increase in temperature, the pore size increased, and the ion diffusion resistance decreased, causing the CV curve to approach a rectangular shape. However, a comparison of the samples shows that the rectangular area of LLPC-800-1:3 was the largest, indicating the largest specific capacitance. At scan rates ranging from 10 to 200 mV s^{-1} , the CV curves of LLPC-800-1:3 (Fig. 5b) became increasingly deformed as the scan rate increased. The stored charge

was attributed to the double-layer formation mechanism [57]. Even at a scan rate of 200 mV s^{-1} , the CV curve of the material was rectangular, indicating its good rate performance as a supercapacitor material. The CV curves of LLPC-800-1:2 and LLPC-800-1:4 are shown in Fig. S4. Fig. 5c shows the galvanostatic charge/discharge (GCD) curves of LLPC at a current density of 1 A g^{-1} . The GCD curves of the LLPC are observed to form a nearly symmetrical triangle. A transition zone is observed between -1 and 0.4 V , which is consistent with the position of the bulge in the CV curves and

Table 3

Comparison of the electrochemical performance of ACs from different biomass precursors.

Precursor	Electrolyte	Electrode system	Current density	Cg/(F g ⁻¹)	Reference
willow catkin	6 M KOH	3-electrode	0.5 A g ⁻¹	298	[58]
tobacco rods	6 M KOH	3-electrode	0.5 A g ⁻¹	286.6	[59]
pomelo peel	6 M KOH	3-electrode	1 A g ⁻¹	289	[60]
silkworm	6 M KOH	3-electrode	1 A g ⁻¹	304	[61]
shiitake mushroom	6 M KOH	3-electrode	1 A g ⁻¹	306	[62]
broad bean shell	6 M KOH	3-electrode	0.5 A g ⁻¹	202	[63]
sugar cane bagasse	6 M KOH	3-electrode	1 A g ⁻¹	323	[64]
Brussel sprouts	6 M KOH	3-electrode	0.5 A g ⁻¹	255	[65]
lotus leaf	6 M KOH	3-electrode	1 A g ⁻¹	379	This work

may be due to heteroatom doping. As the temperature increased, the specific capacitance increased first and then decreased, which is consistent with the trend observed for the rectangular area of the CV curves with changing temperature. Fig. 5d shows the GCD curves of LLPC-800-1:3 at current densities between 1 and 20 A g⁻¹; nearly all of the curves form isosceles triangles. At a current density of 10 A g⁻¹, the IR drop was calculated to be only 39 mV, indicating a low equivalent series resistance. The GCD curves of LLPC-800-1:2 and LLPC-800-1:4 are shown in Fig. S5.

The specific capacitance values of the LLPC were calculated over the current density range of 1–30 A g⁻¹ (Fig. 5e). The specific capacitance of the LLPC decreased as the current density increased because raising the current density increased the resistance to charge diffusion in the pores. At a current density of 1 A g⁻¹, the specific capacitances of LLPC-700-1:3, LLPC-800-1:3 and LLPC-900-

1:3 were 344 F g⁻¹, 379 F g⁻¹ and 286 F g⁻¹, respectively. At a high current density of 20 A g⁻¹, the specific capacitances of the three samples remained 260 F g⁻¹, 298 F g⁻¹ and 232 F g⁻¹, respectively. In addition, the capacitance retention rates of LLPC-700-1:3, LLPC-800-1:3 and LLPC-900-1:3 were 76%, 79% and 81%, respectively. The specific capacitances of LLPC-800-1:2 and LLPC-800-1:4 were 345 F g⁻¹ and 347 F g⁻¹, respectively. At a high current density of 20 A g⁻¹, the capacitance retention rates of LLPC-800-1:2 and LLPC-800-1:4 were 83% and 76%, respectively. These results indicate that LLPC-800-1:3 exhibits better performance than other biomass-derived carbon materials used for supercapacitor electrodes. As shown in Table 3, compared with AC prepared from other biomass types, such as shiitake mushrooms, rice husk and sugar cane bagasse [58–65], the LLPC material shows enhanced performance. Fig. 5f is a Nyquist plot of the material measured by electrochemical

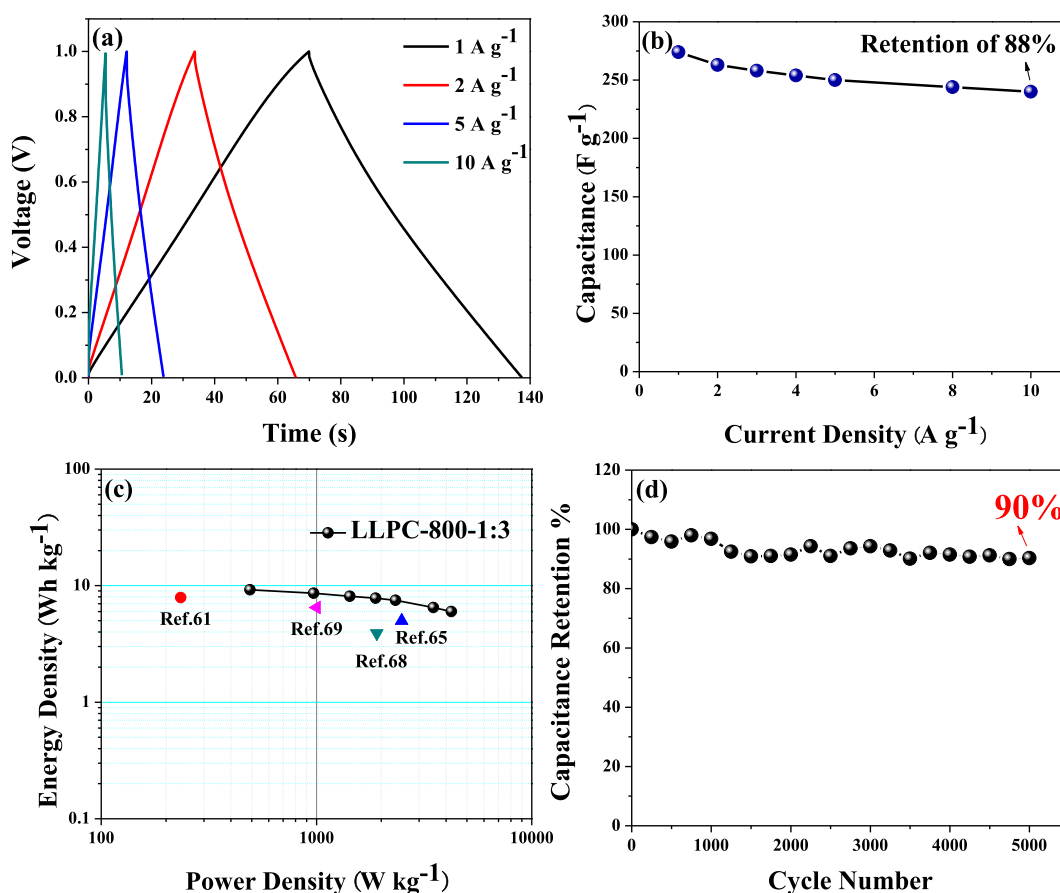


Fig. 6. Electrochemical performance of LLPC-800-1:3 measured in a two-electrode system in 6 M KOH electrolyte: (a) GCD curves at different current densities; (b) specific capacitances for a single electrode at different current densities; (c) Ragone plot of the symmetrical system; and (d) cycling stability at a current density of 5 A g⁻¹.

impedance spectroscopy (EIS) over a frequency range of 10 mHz–100 kHz. With increasing activation temperature, the slope of the impedance curve, and the line approaches the imaginary axis. This observation implies that the material has a low diffusion resistance in the pores, indicating the good electrical properties of the material. The inset is a magnified spectrum in the high-frequency region, and the R_s values of LLPC-700-1:3, LLPC-800-1:3 and LLPC-900-1:3 were calculated to be 0.66 Ω , 0.70 Ω and 0.73 Ω , respectively, depending on the span of the arc. Moreover, the R_s values of LLPC-800-1:2 and LLPC-800-1:4 were calculated to be 0.59 Ω and 0.63 Ω , respectively, depending on the span of the arc. The semicircle in the high-frequency region should be related to the Faraday process of charge transfer at the electrode/electrolyte interface [66]. The 45-degree diagonal part is called the Warburg resistance, which corresponds to the ion diffusion resistance of the electrode. LLPC-800-1:3 exhibits Warburg lines that are shorter than those of the other LLPCs; thus, the material shows a good ion diffusion.

The performed comparison described above demonstrates that the electrochemical performance of LLPC-800-1:3 was the best among the different LLPCs. A symmetrical double-electrode system consisting of two electrodes of the same size was therefore used to further characterize the electrochemical performance of LLPC-800-1:3 in 6 M KOH. In Fig. 6a, the GCD curve of LLPC-800-1:3 shows a typical isosceles triangle, and the shape of the triangle is slightly deformed, which is due to the formation of a pseudocapacitor by the redox reaction. Fig. 6b shows the specific capacitance calculated for a single electrode. At 1 A g⁻¹, the specific capacitance of LLPC-

800-1:3 was 274 F g⁻¹. Even when the current density increased to 10 A g⁻¹, the specific capacitance remained stable at 240 F g⁻¹, and the capacitance retention rate was 88%. The electrode's performance is significantly better than that of the materials derived from silkworm (235 F g⁻¹ at 1 A g⁻¹), starch (234 F g⁻¹ at 2 A g⁻¹) and other biomass carbon sources [61,67]. As a test electrode material for supercapacitors, LLPC-800-1:3 exhibits excellent electrochemical performance. Fig. 6c is a Ragone plot of a symmetrical supercapacitor, in which the energy density of the electrode is 9.2 W h kg⁻¹ and the power density is 491 W kg⁻¹. When the energy density is 7.5 W h kg⁻¹, the power density reaches 2328 W kg⁻¹. The power density and energy density of LLPC-800-1:3 are higher than those reported previously for materials derived from silkworms, cabbage and other carbon sources [61,65,68,69], mainly due to the effect of the oxygen functional groups on the surface of the material. Fig. 6d shows the cycling stability test results of LLPC-800-1:3. At a current density of 5 A g⁻¹, the capacitance of the material remained 90% of the initial capacitance after 5000 cycles. The material therefore exhibits extremely high cycling stability. The decrease in capacitance was due to deactivation of the oxygen-containing functional groups on the surface of the activated carbon material.

The electrochemical performance of the material was measured by using 1 M Na₂SO₄ as the electrolyte in the double-electrode system. Fig. 7a shows the CV curves for LLPC-800-1:3 at a scan rate of 20 mV s⁻¹ and a different voltage range (1 V–1.8 V). The CV curves do not contain a redox peak, indicating that the material does not participate in a redox reaction. Fig. 7b presents the GCD

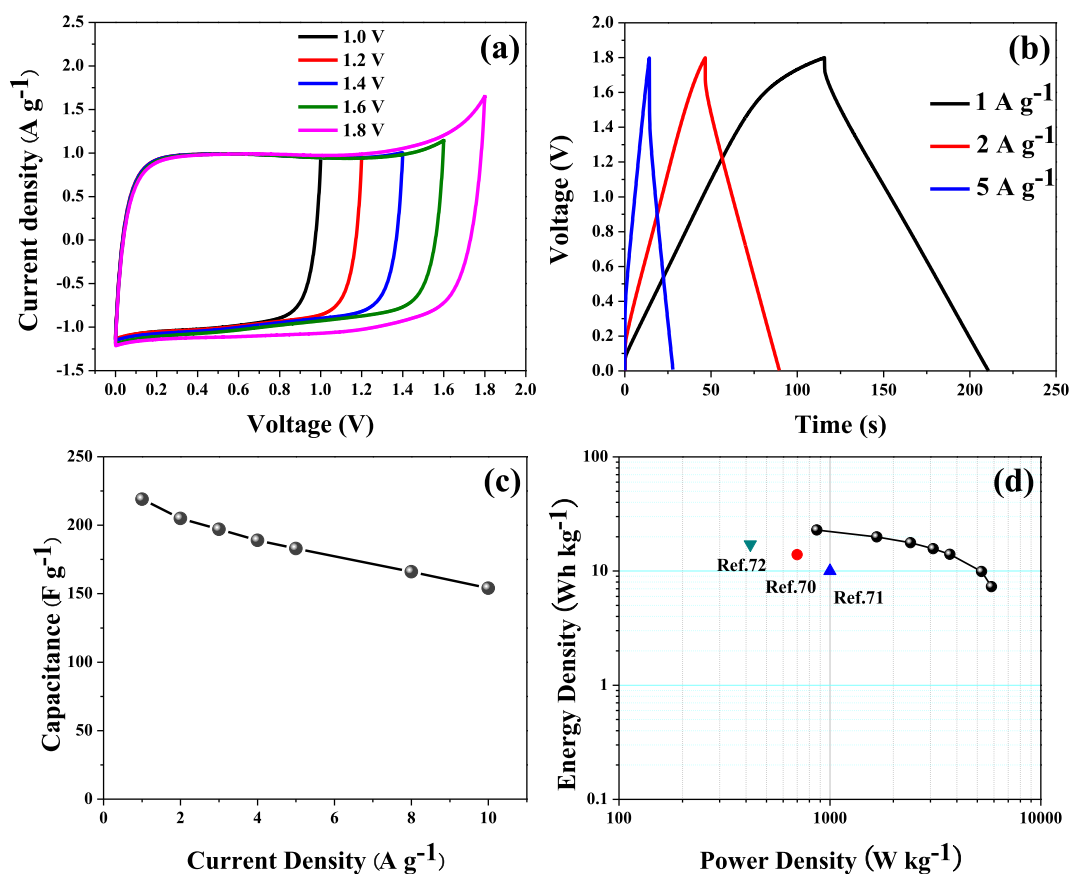


Fig. 7. Electrochemical measurements of the assembled LLPC-800-1:3//LLPC-800-1:3 symmetric supercapacitor in 1 M Na₂SO₄ electrolyte: (a) CV curves of the cell operated in different voltage windows at a scan rate of 20 mV s⁻¹; (b) GCD curves of the cell at various current densities; (c) specific capacitances for a single electrode at different current densities; and (d) Ragone plot of LLPC-800-1:3.

curves of LLPC-800-1:3 at different current densities, approximating the shape of an isosceles triangle, which indicates that the material exhibits good electrochemical reversibility. Fig. 7c shows the specific capacitance of the LLPC-800-1:3 single electrode at different current densities. The specific capacitance reached 219 F g^{-1} at 1 A g^{-1} , and at a current density of 10 A g^{-1} , the specific capacitance was 154 F g^{-1} . The capacitance retention rate reached 70%. Fig. 7d is a Ragone diagram of a symmetric supercapacitor. At an energy density of 23 Wh kg^{-1} , the power density reached 868 W kg^{-1} . Compared with previously reported supercapacitor materials using $1 \text{ M Na}_2\text{SO}_4$ as the electrolyte [70–72], the LLPC-800-1:3 material is an excellent electrode material for supercapacitors with high power density and high energy density.

4. Conclusions

In conclusion, we used renewable lotus leaf biomass to successfully produce AC with a high SSA by carbonization and KOH activation. By adjusting the activation temperature, we determined that LLPC exhibited the best performance when calcined at 800°C . LLPC-800-1:3, which was prepared at that temperature, provided a capacitance of 379 F g^{-1} at 1 A g^{-1} and a capacitance of 298 F g^{-1} at a high current density of 20 A g^{-1} . In addition, the material showed good cycling stability, and after 5000 charging/discharging cycles, the capacitance retention rate reached 90%. When the energy density of the electrode was high, i.e., 9.2 Wh kg^{-1} , the power density was 491 W kg^{-1} . When the voltage was 1.8 V and $1 \text{ M Na}_2\text{SO}_4$ was the aqueous electrolyte, the power density was 868 W kg^{-1} , demonstrating a high energy density of 23 Wh kg^{-1} . These results show that, as a supercapacitor electrode, the LLPC has a great potential for practical applications.

Acknowledgements

This work was supported by the National Natural Science Foundation of China (21406056), Heilongjiang Natural Science Foundation (B2017011) and Funds for Innovative Research Projects of Graduate Students of Heilongjiang University (YJSCX2017-058HLJU).

Appendix A. Supplementary data

Supplementary data related to this article can be found at <https://doi.org/10.1016/j.jallcom.2018.04.123>.

References

- [1] Q. Ma, Y. Yu, M. Sindoro, A. Fane, R. Wang, H. Zhang, Carbon-based functional materials derived from waste for water remediation and energy storage, *Adv. Mater.* (2017) 1605361. <https://doi.org/10.1002/adma.201605361>.
- [2] J. Wang, P. Nie, B. Ding, S. Dong, X. Hao, H. Dou, X. Zhang, Biomass derived carbon for energy storage devices, *J. Mater. Chem. A* 5 (2017) 2411–2428.
- [3] L. Zhang, X. Zhao, Carbon-based materials as supercapacitor electrodes, *Chem. Soc. Rev.* 38 (2009) 2520–2531.
- [4] L. Liu, Z. Niu, J. Chen, Unconventional supercapacitor from nanocarbon-based electrode materials to device configurations, *Chem. Soc. Rev.* 45 (2016) 4340–4363.
- [5] Y. Wang, Y. Song, Y. Xia, Electrochemical capacitors: mechanism, materials, systems, characterization and applications, *Chem. Soc. Rev.* 45 (2016) 5925–5950.
- [6] Y. Cai, Y. Luo, H. Dong, X. Zhao, Y. Xiao, Y. Liang, H. Hu, Y. Liu, M. Zheng, Hierarchically porous carbon nanosheets derived from *Moringa oleifera* stems as electrode material for high-performance electric double-layer capacitors, *J. Power Sources* 353 (2017) 260–269.
- [7] P. Simon, Y. Gogotsi, Materials for electrochemical capacitors, *Nat. Mater.* 7 (2008) 845–854.
- [8] F. Béguin, V. Presser, A. Balducci, E. Frackowiak, Carbons and electrolytes for advanced supercapacitor, *Adv. Mater.* 26 (2014) 2219–2251.
- [9] Y. Cai, Y. Luo, Y. Xiao, X. Zhao, Y. Liang, H. Hu, H. Dong, L. Sun, Y. Liu, M. Zheng, Facile synthesis of three-dimensional heteroatom-doped and hierarchical egg-box-like carbons derived from *moringa oleifera* branches for high-performance supercapacitor, *ACS Appl. Mater. Interfaces* 8 (2016) 33060–33071.
- [10] H. Sun, W. He, C. Zong, L. Lu, Template-free synthesis of renewable macroporous carbon via yeast cells for high-performance supercapacitor electrode materials, *ACS Appl. Mater. Interfaces* 5 (2013) 2261–2268.
- [11] J. Huang, Y. Liang, H. Hu, S. Liu, Y. Cai, H. Dong, M. Zheng, Y. Xiao, Y. Liu, Ultrahigh-surface-area hierarchical porous carbon from chitosan: acetic acid mediated efficient synthesis and its application in superior supercapacitor, *J. Mater. Chem. A* 5 (2017) 24775–24781.
- [12] L. Wang, Q. Zhang, S. Chen, F. Xu, S. Chen, J. Jia, H. Tan, H. Hou, Y. Song, Electrochemical sensing and biosensing platform based on biomass-derived macroporous carbon materials, *Anal. Chem.* 86 (2014) 1414–1421.
- [13] W. Qian, F. Sun, Y. Xu, L. Qiu, C. Liu, S. Wang, F. Yan, Human hair-derived carbon flakes for electrochemical supercapacitor, *Energy Environ. Sci.* 7 (2014) 379–386.
- [14] L. Wang, Z. Gao, J. Chang, X. Liu, D. Wu, F. Xu, Y. Guo, K. Jiang, Nitrogen-Doped porous carbons as electrode materials for high performance supercapacitor and dye-sensitized solar cell, *ACS Appl. Mater. Interfaces* 7 (2015) 20234–20244.
- [15] J. Yan, Q. Wang, T. Wei, L. Jiang, M. Zhang, X. Jing, Z. Fan, Template-Assisted low temperature synthesis of functionalized graphene for ultrahigh volumetric performance supercapacitor, *ACS Nano* 8 (2014) 4720–4729.
- [16] J.P. Paraknowitsch, A. Thomas, Doping carbons beyond nitrogen: an overview of advanced heteroatom doped carbons with boron, sulphur and phosphorus for energy applications, *Energy Environ. Sci.* 6 (2013) 2839–2855.
- [17] L. Wang, Q. Zhang, S. Chen, F. Xu, S. Chen, J. Jia, H. Tan, H. Hou, Y. Song, Electrochemical sensing and biosensing platform based on biomass-derived macroporous carbon materials, *Anal. Chem.* 86 (2014) 1414–1421.
- [18] Y.S. Yun, S.Y. Cho, J. Shim, B.H. Kim, S.J. Chang, S.J. Baek, Y.S. Huh, Y. Tak, Y.W. Park, S. Park, H.J. Jin, Microporous carbon nanoflakes from regenerated silk proteins for supercapacitor, *Adv. Mater.* 25 (2013) 1993–1998.
- [19] J. Yang, S. Gunasekaran, Electrochemically reduced graphene oxide sheets for use in high performance supercapacitor, *Carbon* 51 (2013) 36–44.
- [20] M. Wang, L.D. Duong, N.T. Mai, S. Kim, Y. Kim, H. Seo, Y.C. Kim, W. Jang, Y. Lee, J. Suhr, J.-D. Nam, All-solid-state reduced graphene oxide supercapacitor with large volumetric capacitance and ultralong stability prepared by electrophoretic deposition method, *ACS Appl. Mater. Inter.* 7 (2015) 1348–1354.
- [21] A.R. John, P. Arumugam, Open ended nitrogen-doped carbon nanotubes for the electrochemical storage of energy in a supercapacitor electrode, *J. Power Sources* 277 (2015) 387–392.
- [22] K. Shi, I. Zhitomirsky, Asymmetric supercapacitor based on activated-carbon-coated carbon nanotubes, *ChemElectroChem* 2 (2015) 396–403.
- [23] A. Izadi-Najafabadi, T. Yamada, D.N. Futaba, M. Yudasaka, H. Takagi, H. Hatori, S. Iijima, K. Hata, High-power supercapacitor electrodes from single-walled carbon nanohorn/nanotube composite, *ACS Nano* 5 (2011) 811–819.
- [24] W. Li, F. Zhang, Y. Dou, Z. Wu, H. Liu, X. Qian, D. Gu, Y. Xia, B. Tu, D. Zhao, A self-template strategy for the synthesis of mesoporous carbon nanofibers as advanced supercapacitor electrodes, *Adv. Energy Mater.* 1 (2011) 382–386.
- [25] Z. Wang, Y. Xiong, S. Guan, A simple CaCO_3 -assisted template carbonization method for producing nitrogen doped porous carbons as electrode materials for supercapacitor, *Electrochim. Acta* 188 (2016) 757–766.
- [26] M. Sevilla, R. Mokaya, Energy storage applications of activated carbons: supercapacitor and hydrogen storage, *Energy Environ. Sci.* 7 (2014) 1250–1280.
- [27] D. Hulicova-Jurcakova, M. Seredych, G.Q. Lu, T.J. Bandoz, Combined effect of nitrogen- and oxygen-containing functional groups of microporous activated carbon on its electrochemical performance in supercapacitor, *Adv. Funct. Mater.* 19 (2009) 438–447.
- [28] K. Wang, R. Yan, N. Zhao, X. Tian, X. Li, S. Lei, Y. Song, Q. Guo, L. Liu, Bio-inspired hollow activated carbon microtubes derived from willow catkins for supercapacitor with high volumetric performance, *Mater. Lett.* 174 (2016) 249–252.
- [29] F. Gao, J.Y. Qu, Z.B. Zhao, Z.Y. Wang, J.S. Qiu, Nitrogen-doped activated carbon derived from prawn shells for high-performance supercapacitor, *Electrochim. Acta* 190 (2016) 1134–1141.
- [30] D. Momodu, M. Madito, F. Barzegar, A. Bello, A. Khaleed, O. Olaniyan, J. Dangbegnon, N. Manyala, Activated carbon derived from tree bark biomass with promising material properties for supercapacitor, *J. Solid State Electrochem.* 21 (2017) 859–872.
- [31] E. Hao, W. Liu, S. Liu, Y. Zhang, H. Wang, S. Chen, F. Cheng, S. Zhao, H. Yang, Rich sulfur doped porous carbon materials derived from ginkgo leaves for multiple electrochemical energy storage devices, *J. Mater. Chem. A* 5 (2017) 2204–2214.
- [32] Q. Liang, L. Ye, Z. Huang, Q. Xu, Y. Bai, F. Kang, Q. Yang, A honeycomb-like porous carbon derived from pomelo peel for use in high-performance supercapacitor, *Nanoscale* 6 (2014) 13831–13837.
- [33] H. Feng, M. Zheng, H. Dong, Y. Xiao, H. Hu, Z. Sun, C. Long, Y. Cai, X. Zhao, H. Zhang, B. Lei, Y. Liu, Three-dimensional honeycomb-like hierarchically structured carbon for high-performance supercapacitors derived from high-ash-content sewage sludge, *J. Mater. Chem. A* 3 (2015) 15225–15234.
- [34] H. Feng, H. Hu, H. Dong, Y. Xiao, Y. Cai, B. Lei, Y. Liu, M. Zheng, Hierarchical structured carbon derived from bagasse wastes: a simple and efficient synthesis route and its improved electrochemical properties for high-performance supercapacitors, *J. Power Sources* 302 (2016) 164–173.

- [35] S. Dutta, A. Bhaumik, K.C.-W. Wu, Hierarchically porous carbon derived from polymers and biomass: effect of interconnected pores on energy applications, *Energy Environ. Sci.* 7 (2014) 3574–3592.
- [36] Z. Zhao, S. Hao, P. Hao, Y. Sang, A. Manivannan, N. Wu, H. Liu, Lignosulphonate-cellulose derived porous activated carbon for supercapacitor electrode, *J. Mater. Chem. A* 3 (2015) 15049–15056.
- [37] Y. Li, Y. Pi, L. Lu, S. Xu, T. Ren, Hierarchical porous active carbon from fallen leaves by synergy of K_2CO_3 and their supercapacitor performance, *J. Power Sources* 299 (2015) 519–528.
- [38] J. Deng, M. Li, Y. Wang, Biomass-derived carbon: synthesis and applications in energy storage and conversion, *Green Chem.* 18 (2016) 4824–4854.
- [39] M. Zhang, X. Jin, L. Wang, M. Sun, Y. Tang, Y. Chen, Y. Sun, X. Yang, P. Wan, Improving biomass-derived carbon by activation with nitrogen and cobalt for supercapacitor and oxygen reduction reaction, *Appl. Surf. Sci.* 411 (2017) 251–260.
- [40] M. Enterría, F. Martín-Jimeno, F. Suarez-García, J. Paredes, M. Pereira, J. Martins, A. Martínez-Alonso, J. Tascon, J. Figueiredo, Effect of nanostructure on the supercapacitor performance of activated carbon xerogels obtained from hydrothermally carbonized glucose-graphene oxide hybrids, *Carbon* 105 (2016) 474–483.
- [41] F. Yang, L. Sun, W. Xie, Q. Jiang, Y. Gao, W. Zhang, Y. Zhang, Nitrogen-functionalization biochars derived from wheat straws via molten salt synthesis: an efficient adsorbent for atrazine removal, *Sci. Total Environ.* 607 (2017) 1391–1399.
- [42] L. Wang, X. Jiao, P. Liu, Y. Ouyang, X. Xia, W. Lei, Q. Hao, Self-template synthesis of yolk-shelled $NiCo_2O_4$ spheres for enhanced hybrid supercapacitors, *Appl. Surf. Sci.* 427 (2018) 174–181.
- [43] S. Song, F. Ma, G. Wu, D. Ma, W. Geng, J. Wan, Facile self-templating large scale preparation of biomass-derived 3D hierarchical porous carbon for advanced supercapacitor, *J. Mater. Chem. A* 3 (2015) 18154–18162.
- [44] D. Ma, G. Wu, J. Wan, F. Ma, W. Geng, S. Song, Oxygen-enriched hierarchical porous carbon derived from biowaste sunflower heads for high-performance supercapacitor, *RSC Adv.* 5 (2015) 107785–107792.
- [45] H. Shin, S. Jeon, S.S. Im, CNT/PEDOT core/shell nanostructures as a counter electrode for dye-sensitized solar cells, *Synth. Met.* 161 (2011) 1284–1288.
- [46] J. Shao, F. Ma, G. Wu, C. Dai, W. Geng, S. Song, J. Wan, In-situ MgO ($CaCO_3$) templating coupled with KOH activation strategy for high yield preparation of various porous carbons as supercapacitor electrode materials, *Chem. Eng. J.* 321 (2017) 301–313.
- [47] A. Janes, T. Thomborg, H. Kurig, E. Lust, Nanoscale fine-tuning of porosity of carbide-derived carbon prepared from molybdenum carbide, *Carbon* 47 (2009) 23–29.
- [48] X. Gao, W. Xing, J. Zhou, G. Wang, S. Zhuo, Z. Liu, Q. Xue, Z. Yan, Superior capacitive performance of active carbons derived from *Enteromorpha prolifera*, *Electrochim. Acta* 133 (2014) 459–466.
- [49] J. Shao, F. Ma, G. Wu, W. Geng, S. Song, J. Wan, D. Ma, Facile preparation of 3D nanostructured O/N co-doped porous carbon constructed by interconnected carbon nanosheets for excellent-performance supercapacitor, *Electrochim. Acta* 222 (2016) 793–805.
- [50] K. Sun, S. Yu, Z. Hu, Z. Li, G. Lei, Q. Xiao, Y. Ding, Oxygen-containing hierarchically porous carbon materials derived from wild jujube pit for high-performance supercapacitor, *Electrochim. Acta* 231 (2017) 417–428.
- [51] U.N. Maiti, J. Lim, K.E. Lee, W.J. Lee, S.O. Kim, Three-dimensional shape engineered, interfacial gelation of reduced graphene oxide for high rate, large capacity supercapacitor, *Adv. Mater.* 26 (2014) 615–619.
- [52] D. Yang, L. Zhou, L. Chen, B. Zhao, J. Zhang, C. Li, Chemically modified graphene oxides as a hole transport layer in organic solar cells, *Chem. Commun.* 48 (2012) 8078–8080.
- [53] S. Zhou, H. Zhang, Q. Zhao, X. Wang, J. Li, F. Wang, Graphene-wrapped polyaniline nanofibers as electrode materials for organic supercapacitor, *Carbon* 52 (2013) 440–450.
- [54] K. Kim, Y. Kim, J. Kim, M. Park, The effects of surface modification on carbon felt electrodes for use in vanadium redox flow batteries, *Mater. Chem. Phys.* 131 (2011) 547–553.
- [55] A. Abdureyym, K. Okudaira, Y. Harada, S. Masuda, M. Aoki, K. Seki, E. Ito, N. Ueno, Characterization of 4-mercaptohydrocinnamic acid self-assembled film on Au(111) by means of X-ray photoelectron spectroscopy, *J. Electron. Spectrosc. Relat. Phenom.* 114–116 (2001) 371–374.
- [56] L. Fan, S. Qiao, W. Song, M. Wu, X. He, X. Qu, Effects of the functional groups on the electrochemical properties of ordered porous carbon for supercapacitor, *Electrochim. Acta* 105 (2013) 299–304.
- [57] Y. Li, Y. Pi, L. Lu, S. Xu, T. Ren, Hierarchical porous active carbon from fallen leaves by synergy of K_2CO_3 and their supercapacitor performance, *J. Power Sources* 299 (2015) 519–528.
- [58] Y. Li, G. Wang, T. Wei, Z. Fan, P. Yan, Nitrogen and sulfur co-doped porous carbon nanosheets derived from willow catkin for supercapacitor, *Nano Energy* 19 (2016) 165–175.
- [59] Y. Zhao, M. Lu, P. Tao, Y. Zhang, X. Gong, Z. Yang, G. Zhang, H. Li, Hierarchically porous and heteroatom doped carbon derived from tobacco rods for supercapacitor, *J. Power Sources* 307 (2016) 391–400.
- [60] Q. Liang, L. Ye, Z. Huang, Q. Xu, Y. Bai, F. Kang, Q. Yang, A honeycomb-like porous carbon derived from pomelo peel for use in high-performance supercapacitor, *Nanoscale* 6 (2014) 13831–13837.
- [61] C. Gong, X. Wang, D. Ma, H. Chen, S. Zhang, Z. Liao, Microporous carbon from a biological waste-stiff silkworm for capacitive energy storage, *Electrochim. Acta* 220 (2016) 331–339.
- [62] P. Cheng, S. Gao, P. Zang, X. Yang, Y. Bai, H. Xu, Z. Liu, Z. Lei, Hierarchically porous carbon by activation of shiitake mushroom for capacitive energy storage, *Carbon* 93 (2015) 315–324.
- [63] G. Xu, J. Han, B. Ding, P. Nie, J. Pan, H. Dou, H. Li, X. Zhang, Biomass-derived porous carbon materials with sulfur and nitrogen dual-doping for energy storage, *Green Chem.* 17 (2015) 1668–1674.
- [64] J. Liu, Y. Deng, X. Li, L. Wang, Promising nitrogen-rich porous carbons derived from one-step calcium chloride activation of biomass-based waste for high performance supercapacitor, *ACS Sustain. Chem. Eng.* 4 (2016) 177–187.
- [65] J. Li, G. Zan, Q. Wu, Nitrogen and sulfur self-doped porous carbon from brussel sprouts as electrode materials for high stable supercapacitor, *RSC Adv.* 6 (2016) 57464–57472.
- [66] C. Peng, X.B. Yan, R.T. Wang, J.W. Lang, Y.J. Ou, Q.J. Xue, Promising activated carbons derived from waste tea-leaves and their application in high performance supercapacitor electrodes, *Electrochim. Acta* 87 (2013) 401–408.
- [67] X. Yang, G. Du, L. Zhang, Y. Liu, Preparation of hierarchical porous carbon material derived from starch for high-performance electrochemical capacitor, *Mater. Lett.* 183 (2016) 52–55.
- [68] X. He, N. Zhao, J. Qiu, N. Xiao, M. Yu, C. Yu, X. Zhang, M. Zheng, Synthesis of hierarchical porous carbons for supercapacitor from coal tar pitch with nano- Fe_2O_3 as template and activation agent coupled with KOH activation, *J. Mater. Chem. A* 1 (2013) 9440–9448.
- [69] H. Wang, X. Sun, Z. Liu, Z. Lei, Creation of nanopores on graphene planes with MgO template for preparing high-performance supercapacitor electrodes, *Nanoscale* 6 (2014) 6577–6584.
- [70] G. Sun, B. Li, J. Ran, X. Shen, H. Tong, Three-dimensional hierarchical porous carbon/graphene composites derived from graphene oxide-chitosan hydrogels for high performance supercapacitor, *Electrochim. Acta* 171 (2015) 13–22.
- [71] C. Long, X. Chen, L. Jiang, L. Zhi, Z. Fan, Porous layer-stacking carbon derived from in-built template in biomass for high volumetric performance supercapacitor, *Nano Energy* 12 (2015) 141–151.
- [72] C. Peng, J. Lang, S. Xu, X. Wang, Oxygen-enriched activated carbons from pomelo peel in high energy density supercapacitor, *RSC Adv.* 4 (2014) 54662–54667.